Biol. Cybern. 80, 327–337 (1999)

Biological Cybernetics

Multiple-input, multiple-output system identification for characterization of limb stiffness dynamics

Eric J. Perreault, Robert F. Kirsch, Ana Maria Acosta

Department of Biomedical Engineering, Case Western Reserve University and Cleveland FES Center, Cleveland, Ohio, USA

Received: 24 March 1998 / Accepted in revised form: 16 December 1998

Abstract. This study presents time-domain and frequency-domain, multiple-input, multiple-output (MIMO) linear system identification techniques that can be used to estimate the dynamic endpoint stiffness of a multijoint limb. The stiffness of a joint or limb arises from a number of physiological mechanisms and is thought to play a fundamental role in the control of posture and movement. Estimates of endpoint stiffness can therefore be used to characterize its modulation during physiological tasks and may provide insight into how the nervous system normally controls motor behavior. Previous MIMO stiffness estimates have focused upon the static stiffness components only or assumed simple parametric models with elastic, viscous, and inertial components. The method presented here captures the full stiffness dynamics during a relatively short experimental trial while assuming only that the system is linear for small perturbations. Simulation studies were performed to investigate the performance of this approach under typical experimental conditions. It was found that a linear MIMO description of endpoint stiffness dynamics was sufficient to describe the displacement responses to small stochastic force perturbations. Distortion of these linear estimates by nonlinear centripetal and Coriolis forces was virtually undetectable for these perturbations. The system identification techniques were also found to be robust in the presence of significant output measurement noise and input coupling. These results indicate that the approach described here will allow the estimation of endpoint stiffness dynamics in an experimentally efficient manner with minimal assumptions about the specific form of these properties.

Correspondence to: R.F. Kirsch, Rehabilitation Engineering Center, Hamann 640, MetroHealth Medical Center, Cleveland, OH 44109-1998, USA
(e-mail: rfk3@po.cwru.edu,
Tel.: + 1-216-778-4139, Fax: + 1-216-778-4259)

1 Introduction

The stiffness of a joint or limb arises from a number of physiological mechanisms and is thought to play a fundamental role in the control of posture and movement (Feldman 1966; Hogan 1985). Stiffness determines how strongly external disturbances are rejected during the maintenance of a fixed posture or the execution of a movement. Hence, it is often assumed that stiffness can be used as a measure of motor stability. Stiffness properties also provide a nonrigid interface that is appropriate for stable interactions with both stable and unstable environmental loads (Colgate and Hogan 1988; De Serres and Milner 1991). Thus, understanding the manner in which limb stiffness varies under different conditions can provide an unique perspective into how the nervous system normally controls posture and movement. Furthermore, the stabilizing actions of stiffness properties could be useful in efforts to restore movements in disabled individuals by providing an indication of the effectiveness of rehabilitation interventions such as reconstructive surgery, external orthoses, and/or functional neuromuscular stimulation (Perreault et al. 1997).

Most previous studies examining human stiffness properties have been performed on single joints. However, a number of fundamentally important features of real movements cannot be revealed by single joint studies. In particular, many tasks performed by limbs are specified in terms of the endpoint (e.g., positioning the hand during manipulation tasks), and motions at the joints are usually subservient to these whole-limb functional needs (Morasso 1981). In addition, many muscles cross more than one joint and thus produce moments at several joints simultaneously. Several previous studies have looked at multijoint stiffness properties. The initial work in this area by Mussa-Ivaldi et al. (1985) found that the endpoint stiffness of the human arm in the horizontal plane was primarily 'spring-like' and that limb geometry had a strong effect on the magnitude and directionality of endpoint stiffness. Stiffness was estimated in this study from the steady-state force responses

to a series of separate one-dimensional 'step' perturbations imposed from different directions. Although several pre-perturbation active tasks were performed by the subjects, all stiffness measurements were done with the subjects relaxed (i.e., passive). Several other studies have used similar techniques to examine the effects of external loads (Shadmehr et al. 1993; McIntyre et al. 1996), and modifications have been made to estimate dynamic properties (Dolan et al. 1993; Tsuji et al. 1995; Gomi and Kawato 1997). These studies used methods with three primary limitations. First, the steady-state stiffness estimates employed in most studies ignore the much larger dynamic stiffness components that can strongly resist transient external disturbances. Second, estimates of steady-state stiffness obtained using transient (step or ramp) perturbations require that the subjects 'do not intervene' in response to step or pulse changes in endpoint position for intervals several times longer than voluntary reaction times. Third, those who have examined dynamic endpoint properties (Dolan et al. 1993; Tsuji et al. 1995; Gomi and Kawato 1997) have made *a priori* assumptions about the structure of the endpoint dynamics and then fit parameters to this structure. These models typically assume linear elastic and viscous components as well as inertial contributions at the endpoint. Although single joint estimates indicate that this may be a reasonable assumption for small perturbations during postural conditions, it is unlikely to hold during less constrained experimental conditions (MacNeil et al. 1992; Kirsch and Kearney 1997).

In this paper, we present an alternative approach for identifying multijoint endpoint stiffness properties that addresses the above limitations. The methodology described here differs from previous techniques in that stochastic perturbations, rather than steps or pulses, are used to evoke responses. Such perturbations minimize the likelihood of voluntary reactions because of their random nature. Stochastic planar perturbations imposed at the endpoint also allow the entire stiffness field to be swept during a relatively short experimental trial, rather than requiring separate trials for each perturbation direction of interest. Furthermore, dynamic input-output stiffness properties can be obtained via system identification with very minimal assumptions regarding system structure. We have therefore implemented multiple-input, multiple-output (MIMO) nonparametric system identification routines in both the time and frequency domains to characterize the dynamic endpoint stiffness (DES) opposing these perturbations. These techniques require no *a priori* assumptions about the system structure other than linearity about a given operating point. A simulation study will be presented which demonstrates the robustness of these methods under conditions similar to those expected experimentally, including nonlinearities due to mass-related interjoint coupling, significant correlation between the inputs, and significant measurement noise at the output. The results of these simulations indicate that the presented methods will be well suited to the study of human endpoint dynamics. It should be noted that our description of these techniques will focus upon issues most relevant to the estimation of planar dynamic endpoint stiffness properties. However, the techniques are quite general and can be applied to any quasi-linear system with an arbitrary number of inputs and outputs.

2 MIMO identification algorithms

The nonparametric identification algorithms developed in this paper are applicable to MIMO linear systems. Figure 1a shows the general structure for a linear system with N inputs and M outputs. As shown in Fig. 1b, such a system can be represented by $N \times M$ single-input, single-output (SISO) subsystems describing the contribution of each input to each output. Algorithms presented in this paper estimate the dynamics of these component SISO subsystems using nonparametric MIMO system identification performed in either the time or the frequency domain. Frequency domain identification provides transfer function (TF) estimates for each of the SISO subsystems, while time domain identification provides estimates of the subsystem impulse response functions (IRFs). TFs and IRFs are related by the Fourier transform, but the numerical processes used to estimate each of these quantities and the corresponding estimation errors are somewhat different.

Both the time and frequency domain algorithms estimate the dynamic systems between all inputs and each output. Therefore, they are multiple-input single-output algorithms (MISO). The application of interest in this paper, the estimation of multijoint limb stiffness dynamics, has multiple outputs and therefore, requires the estimation of multiple MISO systems. The presented algorithms estimate these multiple MISO systems simultaneously and hence are described as being MIMO.

2.1 Frequency domain identification

Frequency domain MIMO identification algorithms based upon the input/output auto and cross-spectra have been developed previously (Bendat and Piersol 1986). The relationship between the input auto- and

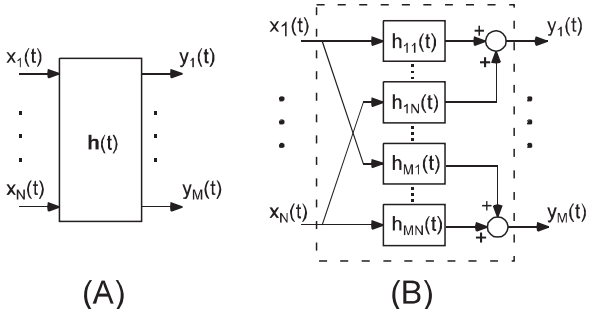

Fig. 1. **A** Block diagram of the structure used to represent a linear multiple-input, multiple-output (MIMO) system with inputs x_i and outputs y_j. **B** Equivalent subsystem representation

cross-spectra and the input/output cross-spectra for a general MIMO system can be described by:

$$G_{x_i y_j}(f) = H_{y_j x_k}(f) \cdot G_{x_i x_k}(f) + \cdots + H_{y_j x_N}(f) \cdot G_{x_i x_N}(f) = \sum_{k=1}^{N} H_{y_j x_k}(f) \cdot G_{x_i x_k}(f) \quad (1)$$

where $G_{x_i x_k}$ is the input cross-spectrum between inputs x_i and x_k, $G_{x_i y_j}$ is the input/output cross-spectra between input x_i and output y_j, and $H_{y_j x_k}$ is the transfer function relating input x_k to output y_j. This equation can be expressed in matrix form as:

$$\begin{bmatrix} G_{x_1 y_1}(f) & \cdots & G_{x_1 y_N}(f) \\ \vdots & \ddots & \\ G_{x_N y_1}(f) & & G_{x_N y_M}(f) \end{bmatrix} = \begin{bmatrix} G_{x_1 x_1}(f) & \cdots & G_{x_1 x_N}(f) \\ \vdots & \ddots & \\ G_{x_N x_1}(f) & & G_{x_N x_M}(f) \end{bmatrix} \times \begin{bmatrix} H_{y_1 x_1}(f) & \cdots & H_{y_M x_1}(f) \\ \vdots & \ddots & \\ H_{y_1 x_N}(f) & & H_{y_M x_N}(f) \end{bmatrix} \quad (2)$$

Solving (2) for the rightmost matrix yields estimates for each of the subsystem transfer functions. The solution for the two-input, two-output system needed to estimate planar DES can be written as:

$$H_{y_j x_1}(f) = \frac{G_{x_1 y_j}(f) \cdot \left[1 - \frac{G_{x_1 x_2}(f) \cdot G_{x_2 y_j}(f)}{G_{x_2 x_2}(f) \cdot G_{x_1 y_j}(f)}\right]}{G_{x_1, x_1}(f) \cdot [1 - \gamma^2_{x_1, x_2}(f)]}$$

$$H_{y_j x_2}(f) = \frac{G_{x_2 y_j}(f) \cdot \left[1 - \frac{G_{x_2 x_1}(f) \cdot G_{x_1 y_j}(f)}{G_{x_1 x_1}(f) \cdot G_{x_2 y_j}(f)}\right]}{G_{x_2, x_2}(f) \cdot [1 - \gamma^2_{x_1, x_2}(f)]} \quad \text{for } j \in [1, 2] \quad (3)$$

where $\gamma^2_{x_1 x_2}(f)$ is the coherence between inputs x_1 and x_2 and is defined as:

$$\gamma^2_{x_1 x_2}(f) = \frac{|G_{x_1 x_2}(f)|^2}{G_{x_1 x_1}(f) \cdot G_{x_2 x_2}(f)} \quad (4)$$

Mutually independent inputs will have a coherence equal to zero; inputs that are perfectly linearly dependent will have a coherence of 1.0. From (3), it is evident that the identification procedure will fail for perfectly coupled inputs (i.e., $\gamma^2_{x_1 x_2} = 1$). If the system inputs are linearly independent (i.e., $\gamma^2_{x_1 x_2} = 0$), the subsystem models can simply be identified individually using SISO identification methods to estimate the linear system between each input and each output. For most experimental situations, $0 < \gamma^2_{x_1 x_2} < 1$, requiring all subsystems to be identified simultaneously, or requiring the inputs to be orthogonalized (Bendat and Piersol 1986).

Multiple coherence functions can be used to investigate the degree to which a given output can be linearly predicted from all of the system inputs and to determine the frequencies over which a linear model can accurately characterize the system dynamics. Regions of low multiple coherence indicate insufficient input power in that frequency range, significant system nonlinearities, noise, or contributions from unmeasured inputs (Marmarelis and Marmarelis 1978). The multiple coherence function for a two-input, two-output system is given by (5). The overbar denotes the complex conjugate operator.

$$\gamma^2_{y_i \cdot x}(f) = \frac{\bar{H}_{y_i x_1}(f) \cdot G_{x_1 y_i}(f) + \bar{H}_{y_i x_2}(f) \cdot G_{x_2 Y_{i2}}(f)}{G_{y_i y_i}(f)} \quad (5)$$

Partial coherence provides an estimate of the linear relationship between one input and one output. These estimates are equivalent to ordinary coherence estimates after the effects of all other inputs have been removed from both the input and output of interest (Bendat and Piersol 1986). The partial coherence functions for a system with two inputs and two outputs is given by:

$$\gamma^2_{x_i y_j \cdot x_k}(f) = \frac{|G_{x_i y_j \cdot x_k}(f)|^2}{G_{x_i x_j \cdot x_k}(f) \cdot G_{y_i y_j \cdot x_k}(f)} \quad \text{for } i, j, k \in [1, 2] \quad \text{and } i \neq k \quad (6)$$

where the residual spectra, $G_{x_i, y_j \cdot x_k}$ are defined as:

$$G_{x_i y_j \cdot x_k}(f) = G_{x_i y_j}(f) \cdot \left[1 - \frac{G_{x_i x_k}(f) \cdot G_{x_k y_j}(f)}{G_{x_k x_k}(f) \cdot G_{x_i y_j}(f)}\right] \quad (7)$$

The auto- and cross-spectral functions, upon which the transfer function estimates are based, are typically estimated from finite data record lengths using the periodogram approach (Welch 1967). However, this estimator of spectral quantities suffers from both random error, due to estimating system properties from a single data record containing random output noise, and bias error, due to the finite record length. Random error is typically minimized by dividing the data into many segments, computing the needed spectral estimate for each segment, and then averaging all individual segment estimates. A larger number of segments thus results in smaller random error and smoother spectral estimates. However, the decrease in the record length for the periodogram resulting from this segmentation procedure can lead to bias error. Excessive segmentation also degrades spectral resolution, since the two are inversely related. These issues are particularly relevant for the computation of DES, which has a bandwidth typically less than 3 Hz and thus requires a spectral resolution significantly less than 1 Hz. Coherence estimates are good indicators of both random and bias errors (Bendat and Piersol 1986) and can be used to help choose an appropriate periodogram window size (see Results).

2.2 Time domain

Nonparametric MIMO system identification can also be performed in the time domain, providing estimates of the subsystem impulse response functions (IRFs). IRFs and TFs provide theoretically equivalent descriptions of

system dynamics, although IRFs more conveniently represent system timing. The goodness of fit of the time domain identification procedures can be summarized by the variance accounted for (VAF) for each of the model outputs, and also by the multiple correlation coefficient (R^2) for the entire model.

The time domain identification algorithms utilize auto- and cross-correlation functions to minimize the effects of output measurement noise. Equation (8) shows the correlation estimates used in this work. These estimates exhibit random and bias errors analogous to spectral estimates, but when the system memory is much shorter than the record length, N, bias errors are negligible and have little effect on the results of the algorithm that follows. In fact, Westwick and Kearney (1997) have shown that biased correlation functions can be used to obtain unbiased IRFs using a SISO version of the algorithm presented in this paper.

$$\phi_{xy}(\tau) = \frac{1}{N}\sum_{k=1}^{N-\tau} x(k)y(k+\tau) \tag{8}$$

Equation (9) describes the input/output cross-correlation function for a system with N inputs. $\phi_{x_ix_k}$ is the input cross-correlation between inputs x_i and x_k, $\phi_{x_iy_j}$ is the input/output cross-correlation between input x_i and output x_j, h_{jk} is the IRF relating input x_k to output y_j, and * represents the convolution operator. Equation (9) is the time domain analog to (1).

$$\begin{aligned}\phi_{x_iy_j}(t) &= h_{j1}(t) * \phi_{x_ix_1}(f) + \cdots + h_{jN}(t) * \phi_{x_ix_N}(t)\\ &= \sum_{k=1}^{N} h_{jk}(t) * \phi_{x_ix_k}(t)\end{aligned} \tag{9}$$

The convolution operation can be accurately approximated by a summation for discrete time signals (assuming an adequate sampling rate), and the resulting sum can be expressed in matrix form. Equation (10) provides this representation for a general 2-sided IRF (Hunter and Kearney 1983).

$$\begin{aligned}h(k) * \phi(k) &\equiv \sum_{j=-P}^{Q} h(j)\phi(j-k) = [\Phi]\cdot[h]\\ &= \begin{bmatrix} \phi(-P) & \phi(-P+1) & \cdots & \phi(Q) \\ \phi(-P-1) & \phi(-P) & & \\ \vdots & & \ddots & \\ \phi(-2P-Q) & & & \phi(-P) \end{bmatrix}\\ &\quad\times \begin{bmatrix} h(-P) \\ h(-P+1) \\ \vdots \\ h(Q) \end{bmatrix}\end{aligned} \tag{10}$$

Substituting (10) into (9) yields the matrix equation for the MIMO cross-correlation function shown in (11).

$$\begin{bmatrix} [\phi_{x_1y_1}] & \cdots & [\phi_{x_1y_M}] \\ \vdots & \ddots & \\ [\phi_{x_Ny_1}] & & [\Phi_{x_Ny_M}] \end{bmatrix} = \begin{bmatrix} [\Phi_{x_1x_1}] & \cdots & [\Phi_{x_1x_N}] \\ \vdots & \ddots & \\ [\Phi_{x_Nx_1}] & & [\Phi_{x_Nx_N}] \end{bmatrix} \times \begin{bmatrix} [h_{11}] & \cdots & [h_{M1}] \\ \vdots & \ddots & \\ [h_{1N}] & & [h_{NM}] \end{bmatrix} = \Psi \cdot H \tag{11}$$

Equation (11) can be solved via matrix inversion to yield the matrix of IRFs, H, describing the system dynamics.

VAF and R^2 can be efficiently estimated from the intermediate results of the time-domain identification. Equation (12) shows the VAF estimate for each model output, while (13) describes the estimate of R^2. The derivation of these quantities is presented in the Appendix.

$$\begin{aligned}\mathrm{VAF}_{y_i} &\equiv \left[1 - \frac{E[(y_i(t) - \hat{y}_i(t))^2]}{E[y_i(t)^2]}\right] \times 100\% \quad \text{for } i \in [1,2]\\ &= \left[\frac{\sum_{j=1}^{N}\sum_{\tau=-P}^{Q} h_{ij}(\tau)\cdot\phi_{x_jy_i}(-\tau)}{E[y_i(t)^2]}\right] \times 100\%\end{aligned} \tag{12}$$

$$\begin{aligned}R^2 &\equiv 1 - \frac{\sum_{i=1}^{M} E[(y_i(t) - \hat{y}_i(t))^2]}{\sum_{i=1}^{M} E[y_i(t)^2]}\\ &= \frac{\sum_{i=1}^{M}\sum_{j=1}^{N}\sum_{\tau=-P}^{Q} h_{ij}(\tau)\cdot\phi_{x_jy_i}(-\tau)}{\sum_{i=1}^{M} E[y_i(t)^2]}\end{aligned} \tag{13}$$

3 Simulation methods

The numerical properties of these algorithms and their usefulness for estimating dynamic endpoint stiffness were investigated via a series of computer simulations of a two-joint dynamic system mimicking the human arm acting in a horizontal plane. One set of simulations was performed using a nonlinear dynamic model that included the nonlinear Coriolis and centripetal coupling moments between the humerus and forearm. Elastic and viscous joint properties, rather than endpoint properties, were assumed. The affects of these joint properties were nonlinearly transformed to the endpoint via the kinematic properties of the arm. The equations used for the nonlinear simulations are shown in (14). The parameters for all simulations were taken from the experimental results of Tsuji et al. (1995).

$$J^T\mathbf{f}_{\text{end}} = M(\boldsymbol{\theta})\,\ddot{\boldsymbol{\theta}} + \mathbf{V}(\boldsymbol{\theta},\dot{\boldsymbol{\theta}}) + \mathbf{B}_{\text{jnt}}\,\dot{\boldsymbol{\theta}} + \mathbf{K}_{\text{jnt}}\boldsymbol{\theta} \tag{14}$$

where J is the Jacobian matrix relating incremental changes in joint space to incremental changes in endpoint space, $\mathbf{f}_{\text{end}}$ is the vector of applied endpoint forces, $\boldsymbol{\theta}$ is the vector of joint angles, M is the joint inertia matrix, $\mathbf{V}$ is the vector of centripetal and Coriolis forces, $\mathbf{B}_{\text{jnt}}$ is the vector of *joint* viscosities, and $\mathbf{K}_{\text{jnt}}$ is the vector of static *joint* stiffnesses.

A second set of simulations was performed with a completely linear model of the endpoint dynamics to evaluate the impact of output measurement noise and input coupling on the ability to accurately identify system properties. This linear model was used to separate these effects from those of the system nonlinearities. The linear simulations assumed that DES could be modeled using inertial, viscous, and elastic parameters of the *endpoint* of the arm as have been identified in previous studies (Dolan et al. 1993; Tsuji et al. 1995). These simulations were performed in endpoint coordinates using (15).

$$[I_{\text{end}}][\ddot{\mathbf{x}}] + [B_{\text{end}}][\dot{\mathbf{x}}] + [K_{\text{end}}][\mathbf{x}] = [\mathbf{f}_{\text{end}}];$$

where

$$[I] = \begin{bmatrix} I_{11} & I_{12} \\ I_{21} & I_{22} \end{bmatrix},\ [B] = \begin{bmatrix} B_{11} & B_{12} \\ B_{21} & B_{22} \end{bmatrix},\ [K] = \begin{bmatrix} K_{11} & K_{12} \\ K_{21} & K_{22} \end{bmatrix} \tag{15}$$

I_{end}, B_{end}, and K_{end} represent the *endpoint* inertia, viscosity, and stiffness matrices in two dimensions; $\mathbf{x}$ is the endpoint displacement vector, and $\mathbf{f}_{\text{end}}$ is the vector of applied endpoint forces.

All simulations were performed in Matlab/Simulink (The Mathworks, Natick, MA) using an adaptive step-size Gear integration routine. Simulated planar stochastic force perturbations with a bandwidth of approximately 9 Hz were used as inputs. Figure 2 shows the input force spectrum used for all simulations. Unless otherwise specified, the force perturbations in the two orthogonal directions were mutually independent. Force perturbations had a peak-to-peak amplitude of approximately 1 N, resulting in endpoint displacements of approximately 1 cm for the chosen simulation parameters. Sixty seconds of data were simulated for each trial. The variable sampling rate results of each simulation were linearly interpolated to yield a final uniform sampling rate of 50 Hz. Note that the system describing the relationship between an imposed force and the resulting displacement is known as dynamic compliance, which is simply the inverse of dynamic stiffness. The results presented below are given in terms of dynamic compliance because force was the controlled variable in these simulations, but they could just as easily be presented in terms of dynamic stiffness.

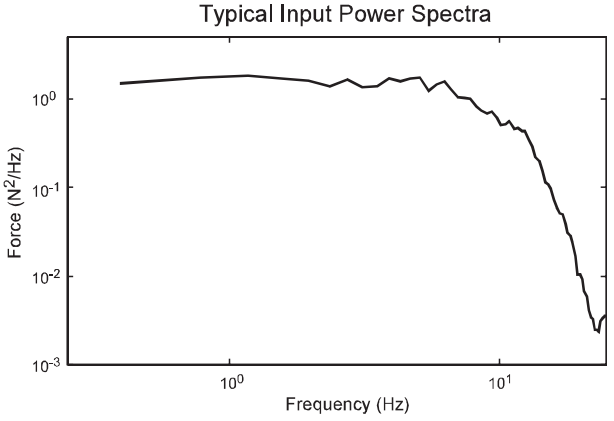

Fig. 2. Typical input force spectra used for all simulations

4 Results

4.1 Linearity

The nonlinear simulations were designed to test the effects of Coriolis and centripetal coupling moments as well as the nonlinear joint-to-endpoint stiffness transformations on the estimation of endpoint dynamics during the application of stochastic endpoint perturbations. Figure 3 shows the magnitude portions of the linear dynamic endpoint compliance TFs estimated from the nonlinear simulation data. These are compared to the theoretical TFs for a linear system described by (15). The linear system used for comparison has no centripetal or Coriolis forces and has endpoint model parameters obtained using the standard transformation shown in (16). Although the Jacobian, J, is a nonlinear function of the joint angles, the endpoint parameter matrices were approximated using the mean joint angle for each simulated trial. Figure 4 illustrates the partial and multiple coherence functions obtained from these nonlinear simulations. All partial and multiple coherences of the nonlinear system remained near 1.0 over the perturbation bandwidth. The slight decrease in the partial coherence of H_{12} is due to estimation bias errors (see *Bias error* section below), not to significant nonlinear contributions. Thus, the nonlinear centripetal and Coriolis coupling moments and the nonlinear joint-to-endpoint transformations appear to have little effect on the overall system linearity during small amplitude stochastic endpoint perturbations.

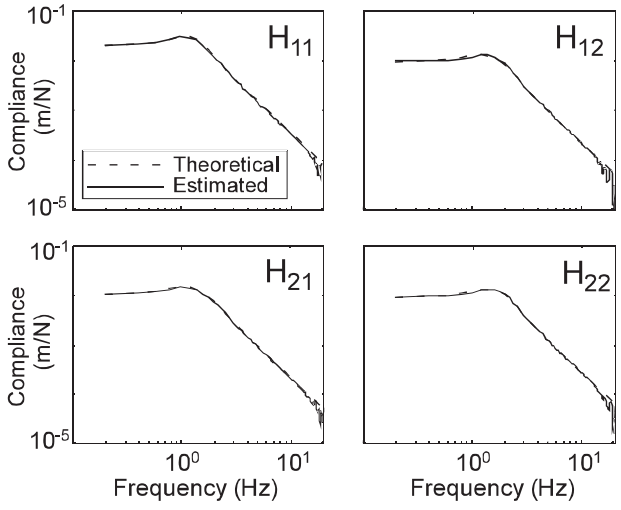

Fig. 3. Comparison of the estimated dynamic endpoint compliance transfer functions (TFs) (____) and those predicted from the known joint stiffnesses (_ _ _ _). Simulation data were obtained using the nonlinear model specified by (13). H_{ji} represents the single-input, single-output (SISO) subsystem between input x_i and output y_j

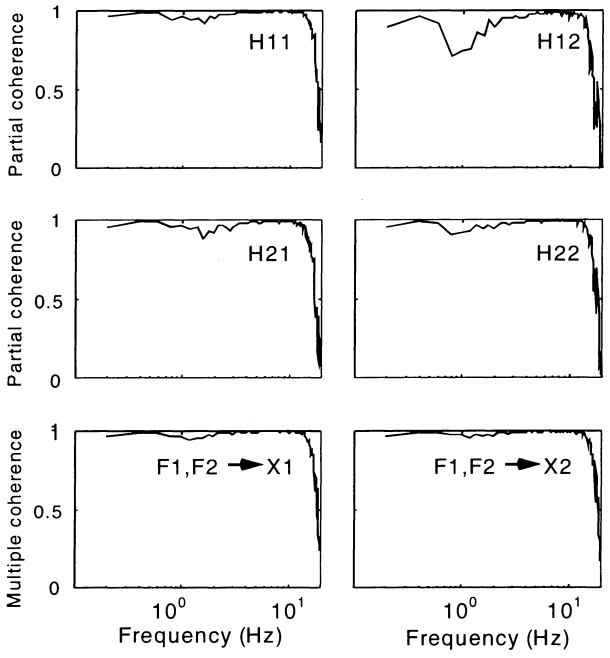

Fig. 4. Coherence estimates for the dynamic compliance estimation. Simulation data were obtained using the nonlinear model specified by (13)

$$K_{\text{end}} = (J^T)^{-1} \cdot K_{\text{jnt}} \cdot J^{-1}$$
$$B_{\text{end}} = (J^T)^{-1} \cdot B_{\text{jnt}} \cdot J^{-1} \quad (16)$$
$$I_{\text{end}} = (J^T)^{-1} \cdot I_{\text{jnt}} \cdot J^{-1}$$

The time domain identification algorithm was used to estimate IRFs from the same nonlinear simulation data. Figure 5 shows the estimated IRFs and those expected from the linear system. The two sets of IRFs in Figure 5 are virtually identical, indicating that the known mechanical nonlinearities of the human arm do not significantly distort the time domain estimation of DES. Time domain results were further used to determine whether the distortion introduced by the nonlinear properties might be more significant at different locations in the workspace. Four locations in the horizontal plane were simulated, corresponding to those measured by Tsuji et al. (1995). All hand locations were in front of the subject; elbow angles ranged from 59° to 126° of flexion, and shoulder angles ranged from 37° to 102° of flexion as measured from the coronal plane. Figure 6 shows that the linear identification procedure was able to account for more than 98% of the output variance at each of the simulated locations. In addition, the estimated IRFs predicted more than 99% of the variance in the simulated IRFs, indicating that the system nonlinearities were insignificant throughout the workspace.

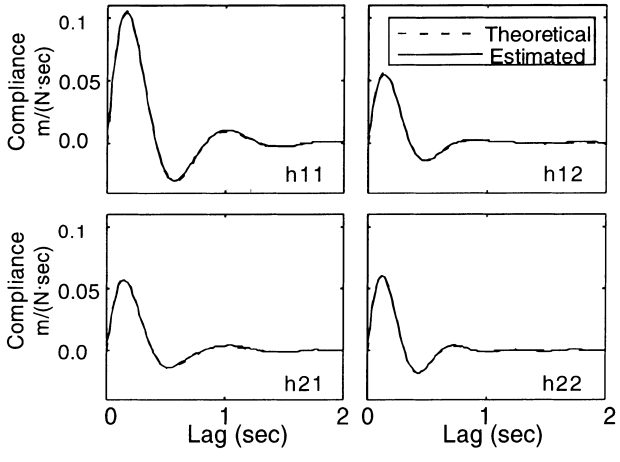

Fig. 5. Comparison of the estimated dynamic compliance impulse response functions (IRFs) (——) and those predicted from the known joint stiffnesses (– – – –). Simulation data were obtained using the nonlinear model specified by (13). h_{ji} represents the SISO subsystem between input x_i and output y_j

4.2 Coupling

The effect of input coupling on the estimation procedure was investigated using data from the linear system simulations. Four different levels of input coupling, from 0% to 75% , were tested. The degree of coupling indicates the percentage of the variance of one input that was linearly related to the second input: 0% coupling indicates completely independent inputs, while 100% coupling represents inputs that are completely linearly dependent. Figure 7 is a conceptual illustration of a system with coupled inputs; Table 1 summarizes the goodness-of-fit of the identification algorithm for different degrees of coupling. The estimated model was able to account for greater than 99% of the output variance at all levels of input coupling. The VAF between the estimated and simulated IRFs decreased slightly at higher coupling levels, but remained above 97% for all trials. These results indicate that the nonparametric linear MIMO identification produced accurate estimates

(A)

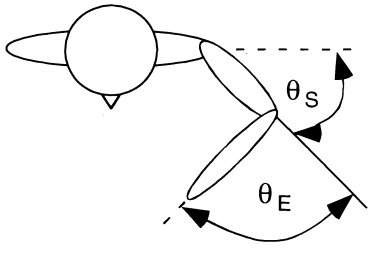

(B)

Location	Θ_S (deg)	Θ_E (deg)	R^2 (%)	VAF (%) between estimated and actual IRFs			
				h11	h12	h21	h22
Position 1	63	77	99.7	99.8	99.6	99.8	99.7
Position 2	42	63	98.8	99.9	99.4	99.4	99.5
Position 3	102	59	99.1	99.8	99.6	99.5	99.6
Position 4	37	127	99.2	99.6	99.3	99.3	99.7

Fig. 6. **A** Definition of upper limb joint angles. **B** Variance accounted for (VAF) between the actual and predicted outputs and between the estimated and expected dynamic compliance IRFs for the simulated nonlinear dynamics at four different locations in the workspace

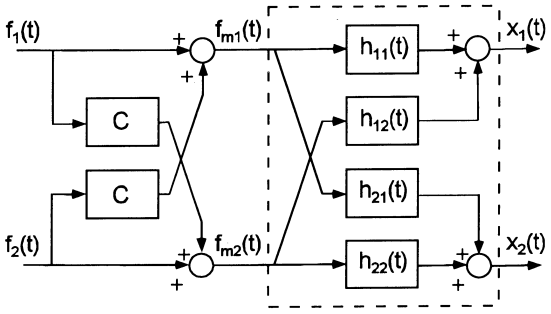

Fig. 7. Schematic of the model used to simulate a system with coupled inputs

Table 1. VAF between the actual and predicted outputs and between the estimated and expected dynamic compliance IRFs at four different levels of input coupling

Coupling (%)	R^2 (%)	VAF (%) between estimated and actual IRFs			
		h11	h12	h21	h22
0	99.8	99.9	99.8	99.8	99.8
25	99.7	99.9	99.6	99.8	99.7
50	99.3	99.7	99.0	99.3	99.4
75	99.3	99.2	97.1	98.5	98.4

of the system dynamics even when the inputs to the system were significantly coupled.

4.3 Noise

The influence of output noise on the estimation procedure was also investigated using data from the linear system simulations. Four output signal-to-noise ratios (SNRs) from 20 to 0 dB (i.e., 10–50% noise) were tested. Figure 8 schematically represents a simulated system with output noise, while Table 2 summarizes the goodness-of-fit of the identification algorithm for different levels of output noise. R^2 decreased monotonically with noise level, which simply reflects the random properties of the noise. More importantly, the goodness-of-fit between the actual and estimated IRFs remained high at all noise levels, indicating that system properties were well characterized by the identification procedure. All the subsystems except for h_{12} showed VAF greater than 90% at all noise levels. Subsystem h_{12} was more poorly identified than the other subsystems because its relative contribution to output y_1 was considerably smaller than that of subsystem h_{11}, while the noise level was identical for both subsystems. Even in this case, the minimum VAF was 81.1% for a 0 dB SNR.

4.4 Bias error

The effects of bias error due to using finite-length data segments to compute spectral quantities were summarized by coherence estimates. These estimates were obtained using data from the linear simulations. Partial

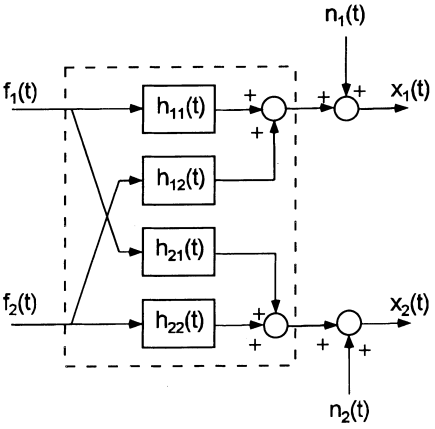

Fig. 8. Schematic of the model used to simulate a system with output measurement noise

Table 2. VAF between the actual and predicted outputs and between the estimated and expected dynamic compliance IRFs at four different signal-to-noise ratios (SNRS)

SNR (dB)	R^2 (%)	VAF (%) between estimated and actual IRFs			
		h11	h12	h21	h22
20	99.1	99.8	99.5	99.8	99.6
10	91.2	99.5	97.5	99.1	98.7
3	67.6	98.1	89.6	96.4	95.2
0	51.4	96.4	81.1	93.2	91.2

and multiple coherences were estimated using Fast Fourier Transform (FFT) segment lengths of 128, 256, and 512 points, corresponding to data segments of duration 2.56, 5.12, and 10.24 s, respectively. The system was simulated with uncoupled inputs and had no output noise, so bias error was the only significant factor reducing coherence below a value of 1.0. Figure 9 shows that the estimated coherence functions were uniformly near 1.0 across the bandwidth of interest for the longest FFT segment length (512 points). However, all coherence functions dropped significantly as the segment length decreased, indicating the presence of significant spectral bias errors. Although these bias errors did not significantly affect the estimated TFs (not shown), the decreased coherence produced by these errors could erroneously be interpreted to represent significant measurement noise or system nonlinearities. Hence, potential bias errors need to be considered when interpreting coherence estimates.

5 Discussion

We have presented two techniques for the identification of MIMO systems and described a number of specific issues related to the use of these techniques in characterizing the endpoint stiffness properties of the human arm. The following paragraphs will discuss the use of these methods and the interpretation of stiffness estimates obtained with them.

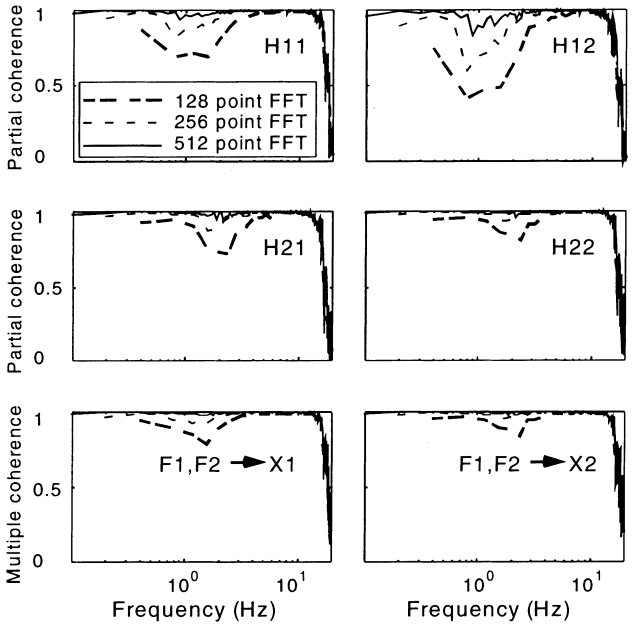

Fig. 9. Estimated partial and multiple coherence functions using FFT window sizes of 128 points (2.56 s; _ _ _ _), 256 points (5.12 s; _ _ _ _), and 512 points (10.24 s; ____)

5.1 Performance of methods and limitations

We have presented both time domain and frequency domain methods for characterizing linear MIMO systems. If data segments of sufficient length are used to minimize the effects of bias error, the performance of each of these methods in characterizing a given linear system is essentially identical. However, the time and frequency domain representations visually and numerically emphasize different aspects of system properties, and thus each may provide unique insights into different features of the system. For example, frequency responses can provide immediate insight into the structure and order of the various subsystems, and the coherences can indicate the presence of excessive noise, biases, and/or nonlinearities. Impulse responses provide a direct indication of the time extent or memory of the system dynamics and can be integrated to generate familiar step responses. VAF and R^2 quantities succinctly summarize the performance of the system identification procedure with a small set of numbers.

In both cases, the applicability of the methods described here is limited to linear systems. However, many conditions of interest will satisfy this condition. Because single-joint stiffness has been found previously to be quite linear for small perturbations (Kearney and Hunter 1990), muscle-related contributions to endpoint stiffness are also expected to be linear. Results from our lab (Perreault et al. 1997) and others (Dolan et al. 1993; Tsuji et al. 1995) indicate this to be the case. Furthermore, the simulations presented in this study have shown that the effects of nonlinear inertial properties and nonlinear joint-to-endpoint transformations are negligible for small stochastic perturbations. Thus, it is expected that the linear approaches presented here will find wide application for limb stiffness estimation over a range of conditions.

The identification algorithms presented were shown to be robust in the presence of significant output noise and for significant input coupling. Measurement noise is impossible to avoid completely in practice, and coupling between inputs during stiffness measurements commonly occurs because of imperfections in multidimensional manipulators. Thus, when purely independent perturbations cannot be imposed, it is not possible to separately identify the properties of the individual subsystems one at a time. Rather, it is necessary to use a MIMO approach similar to the one described here, which simultaneously identifies all subsystems.

It has previously been shown for SISO identification that the IRF estimation error increases when the input spectrum is severely bandlimited (Westwick and Kearney 1997). It is interesting to note that this effect is qualitatively similar to the case of severe input coupling that was tested in this paper. Both input coupling and highly colored inputs add off-diagonal terms to the input correlation matrix, Ψ, given in (11). Therefore, although the presented time domain algorithm was not directly tested for a variety of input spectra, further restricting the input bandwidth can be expected to increase the estimation errors in a manner analogous to increasing the input coupling. Both of these factors serve to increase the IRF estimation error and to amplify the errors introduced by measurement noise. If the errors introduced by either restricted input bandwidth or input coupling become too large for a given level of measurement noise, more robust techniques (Westwick and Kearney 1997) can be employed at the expense of increased computational effort and estimation bias error.

The MIMO system identification procedures outlined above rely upon numerical procedures, the accuracy of which depends upon several practical choices that must be made by the user and built into the experimental design. In particular, both of the methods described here depend upon estimates of input autospectra and input-output cross-spectra. The frequency domain method relies directly on such estimates, while the time-domain method utilizes the closely related auto-correlation and cross-correlation functions. The true spectral quantities are estimated from finite record lengths using the periodogram approach (Welch 1967), but this spectral estimator suffers from both random error and bias error. The effects of random error were investigated using different levels of output noise and were found to be negligible when the experimental trial lengths were sufficiently long to allow for adequate averaging (Table 2). The practical effects of bias error were also presented above (Fig. 9). Bias errors were found to appear mainly in the coherence estimates when short FFT lengths were used; this bias had little effect on the estimated transfer functions. The reduction in coherence resulting from estimation bias could be attributed mistakenly to other causes such as nonlinearities and/or noise. Thus, increasing the number of segments used for averaging can minimize random errors, while increasing the length of the data (FFT) segments minimizes bias errors. The only

solution to these conflicting needs is to design experimental procedures with adequate trial lengths, allowing the recorded data to be sufficiently segmented to reduce random error while keeping the segments long enough to reduce bias error. The presented simulation results indicate that a 60-s trial (22 overlapping FFT segments of 5.12 s each) is sufficient to satisfy these requirements for endpoint identification of the human arm, even under poor experimental conditions (SNR = 0 dB). Better experimental conditions may allow for even shorter experimental trials.

5.2 Multijoint nature of endpoint stiffness

Stiffness has been studied most extensively for single muscles and single joints, and the information that has resulted from these studies forms the basis for much of what is currently understood about the control of posture and movement. Although it is clear that the nervous system modulates stiffness primarily through individual muscle properties, limb stiffness is more than a simple sum of individual muscle or joint properties. At a controller level, most tasks performed by human limbs have goals that require control of the endpoint of the limb, rather than individual control of single muscles or joints. Indeed, the motions at adjacent joints within a limb are often highly coordinated (Soechting and Lacquaniti 1981; Hollerbach and Flash 1982). At a mechanical level, several important multijoint mechanisms influence disturbance resistance and stability. Many muscles span more than one joint, inherently linking the joints together. In addition, the kinematics of the limb (i.e., the geometrical relationship between joint angles and endpoint position) may also play a dominating role in the reflection of individual joint properties at the endpoint (Mussa-Ivaldi et al. 1985; Flash and Mussa-Ivaldi 1990). Much less is known about the relative importance of these multijoint mechanisms, how they interact, and how they are used by the nervous system to control posture and movement. The methods developed here are intended to facilitate efforts to obtain the information necessary to make such assessments. Note that in this paper we have concentrated on a two-dimensional description of endpoint stiffness, primarily because this has been the focus of past studies and because this is what can currently be estimated in our laboratory. However, the identification methods that have been presented here can be used with systems having any number of inputs and outputs, including stiffness estimates in three or higher dimensions.

5.3 Stochastic perturbations and dynamic multijoint stiffness estimates

Many previous studies of multijoint stiffness have been designed to test a particular theory regarding the control of posture and movement, the 'equilibrium point' hypothesis (Mussa-Ivaldi et al. 1985; Flash 1987; Gomi and Kawato 1997) and thus have emphasized the steady-state response to a step perturbation. The steady-state response to a maintained displacement arises primarily from two mechanisms – muscle length-tension properties and the tonic stretch reflex – both of which are typically modest in magnitude relative to the dynamic components resisting an imposed stretch. A portion of the dynamic response is due to viscous muscle properties (Kirsch et al. 1994) and to dynamic reflex activation (Kearney and Stein 1997), but a significant component is the purely passive inertial properties of the limb (Hollerbach and Flash 1982). Furthermore, even the static component of the initial muscle-related response to a perturbation is much larger than the steady-state response due to 'short-range' stiffness effects (Rack and Westbury 1974). Although these effects are transient, they may provide a significant fraction of the resistance to more typical transient disturbances. It is thus entirely possible that dynamic and transient stiffness components are functionally at least as important as steady-state components.

The methods described here use stochastic endpoint perturbations of the limb to estimate its stiffness properties. Such perturbations evoke *both* the dynamic and static mechanisms described above, and the properties evoked by these mechanisms can be quantified by the presented system identification approaches. By using independent stochastic perturbations in each of the endpoint directions of interest, the instantaneous direction of the multidimensional perturbation changes continuously to sweep out the entire stiffness field during a relatively short experimental trial. Because of this experimental efficiency, a number of different conditions can be conveniently examined during a single experimental session. This is in contrast to the standard steady-state stiffness estimation method that uses a number of trials, one for each perturbation direction of interest. Resolution is thus limited by the number of experimental trials, with the additional uncertainty of trial-to-trial variations in subject performance. Furthermore, the number of different conditions that can be tested in one session is significantly reduced because of the number of trials required. Estimation of steady-state stiffness also requires that the subjects 'do not intervene' in response to step or pulse changes in endpoint position for time intervals several times longer than voluntary reaction times. Although this paradigm is widely used, methods for detecting voluntary reactions (which can significantly influence measured stiffness) are subjective and rely primarily on consistency of responses. Interventions that occur in consistent and expected ways cannot be detected. In contrast, stochastic perturbations minimize the likelihood of voluntary reactions due to their inherently random nature. If properly designed, stochastic perturbations can be innocuous and largely ignored by the subjects. In addition, they yield functionally relevant data that are sufficiently rich in information to allow full and experimentally efficient characterization of the limb's directional and dynamic stiffness properties.

5.4 Parametric vs nonparametric stiffness estimation

We have described *nonparametric* methods for characterizing endpoint dynamic stiffness properties, i.e., no particular model structure describing endpoint stiffness has been assumed *a priori*. Our only assumption is that endpoint stiffness is linear for small perturbations and can thus be fully characterized by either its frequency response matrix or its impulse response matrix. This is in contrast to previously used methods for estimating endpoint dynamics (Dolan et al. 1993; Tsuji et al. 1995; Gomi and Kawato 1997), which have assumed a model structure (typically second order) and fit the parameters of this model directly to the data. Based upon previous single-joint studies, it is likely that the assumption of second-order stiffness properties will be reasonably accurate for fixed postural conditions and small perturbations. However, mechanisms certainly exist to make the system non-second-order and/or nonlinear. For example, stiffness estimates are known to vary with perturbation amplitude (Kearney and Hunter 1982) and mean contraction level (Hunter and Kearney 1982) for postural conditions. Furthermore, individual joint stiffnesses have been found to be linear but non-second-order during changing contraction levels (MacNeil et al. 1992) and following a large perturbation (Kirsch and Kearney 1997). Also, stretch reflex responses during perturbations with quite restricted bandwidths produce a nonlinear stiffness component that will not be captured by a second-order model (Kearney and Stein 1997). It is thus unlikely that the second-order description of multijoint endpoint stiffness will survive more general testing. Furthermore, endpoint stiffness has previously been estimated only in the horizontal plane, typically with the weight of the arm supported against gravity, with the implicit assumption that both the elbow and shoulder act as hinge joints. This is obviously a vast simplification for the shoulder, which is actually a complex of several different joints with multiple degrees of freedom. It is thus expected that examination of the endpoint stiffness properties of the arm under more general and realistic conditions will reveal behavior that is of higher order than second.

A nonparametric approach such as the one described here is preferred for exploring a system whose properties are only poorly established. The described approach is capable of assessing the linearity of the measured response (by use of coherence, VAF, or R^2), and the residuals from the linear model can be used to investigate the structure of any existing nonlinearities. If the resulting system is linear, characteristic features of second-order systems, if they actually occur, can be easily detected with either the frequency response or the impulse response. Just as easily, however, non-second-order linear systems of different structure can be recognized. Even if no obvious simple structure is seen in the nonparametric responses, system properties can be usefully described in a functionally relevant but model-independent manner using quantities such as low frequency stiffness, resonant frequency, and damping. Finally, it should again be noted that we have focused upon identification of endpoint stiffness here, although the approach is quite general and can be applied to identify any linear (or linearizable) system with multiple inputs and outputs where no particular model structure is known *a priori*.

6 Conclusions

We have presented a new method for characterizing MIMO dynamic stiffness properties. This approach differs from previous approaches in that stochastic perturbations, rather than steps or pulses, are used to evoke responses. Such perturbations minimize the likelihood of voluntary reactions because of their random nature. Also, independent perturbations imposed in more than one direction at the endpoint result in the entire stiffness field being swept during a relatively short experimental trial, rather than requiring separate trials for each perturbation direction with the accompanying uncertainty of trial-to-trial variations. Furthermore, we have implemented both frequency and time domain identification algorithms that can fully capture both the static and dynamic properties of the perturbation responses without assuming a particular model of these properties (other than linearity) *a priori*.These algorithms were shown to be robust for significant coupling between different inputs (i.e., perturbations in orthogonal endpoint directions) and for significant output noise. Goodness-of-fit measures were presented for both time and frequency domain methods. The effects of nonlinear inertial properties and nonlinear joint-to-endpoint transformations were shown to be negligible for small stochastic perturbations. Finally, the conflicting constraints of short experimental trials versus the need for long data records to reduce estimation bias were discussed.

Acknowledgements We thank the anonymous reviewers for their insightful comments and recommendations. This work was supported by the Department of Veterans Affairs Rehabilitation Research and Development Service, NIH Training Grant 5-T32-GM07535, and a grant from the Whitaker Foundation.

Appendix

Derivation of output VAF estimation

The following derivation assumes that all measured variables are normally distributed with zero mean. Equation (17) defines the variance accounted for between the measured system output, $y_i(t)$, and the estimated output, $\hat{y}_i(t)$.

$$\mathrm{VAF}_{y_i} \equiv \left[1 - \frac{E[(y_i(t) - \hat{y}_i(t)^2]}{E[y_i(t)^2]}\right] \times 100\% \tag{17}$$

The measured output can be described as the sum of the estimated output and a noise term, $e_i(t)$, as shown in (18).

$$y_i = \hat{y}_i + e_i \tag{18}$$

The correlation-based estimates used in this paper provide a solution that is nearly optimal in the least-squares sense. The use of finite length data records causes the estimated IRFs to differ slightly from the least-squares estimates (Marple 1981; Korenberg

1988), but these differences become negligible as the data length increases. Therefore, the residuals, $e_i(t)$, are nearly uncorrelated with the estimated outputs, $\hat{y}_i(t)$. If this correlation is assumed to be negligible, the variance of $e_i(t)$ can be expressed as:

$$E[(y_i(t)-\hat{y}_i(t))^2] = E[y_i(t)^2] - 2E[\hat{y}_i(t)(\hat{y}_i(t)+e_i(t))] + E[\hat{y}_i(t)^2]$$
$$= E[y_i(t)^2] - E[\hat{y}_i(t)^2] \quad (19)$$

Substituting (19) into (17) yields:

$$\mathrm{VAF}_{y_i} = \frac{E[\hat{y}_i(t)^2]}{E[y_i(t)^2]} \times 100\% \quad (20)$$

The expected square value of the estimated output is simply the zero-lag term of the estimated output auto-correlation, as shown in (21).

$$E[\hat{y}_i(t)^2] = \phi_{\hat{y}_i\hat{y}_i}(0) \quad (21)$$

For a MISO system with N inputs and M outputs, the estimated output auto-correlation function is given by (22).

$$\phi_{\hat{y}_i\hat{y}_i} = h_{i1} * \phi_{x_1y_i} + h_{i2} * \phi_{x_2y_i} + \cdots + h_{iN} * \phi_{x_Ny_i} \quad (22)$$

Substituting (22) into (20) provides an efficient means for calculating the VAF for each output of the linear MIMO model.

$$\mathrm{VAF} = \left[\frac{\sum_{i=1}^{N}\sum_{\tau=-P}^{Q} h_{ij}(\tau)\cdot\phi_{x_jy_i}(-\tau)}{E[y_i(t)^2]}\right] \times 100\% \quad (23)$$

Derivation of R^2 estimation

A similar derivation to that outlined above can be used to provide an efficient algorithm for estimating the multiple correlation coefficient, R^2, for a MIMO system. R^2 is defined by (24).

$$R^2 \equiv 1 - \frac{\sum_{i=1}^{M} E[(y_i(t)-\hat{y}_i(t))^2]}{\sum_{i=1}^{M} E[y_i(t)^2]} \quad (24)$$

Substituting the results of (19), (21), and (22) into (24) yields (25). Using (25), R^2 can be efficiently calculated from the intermediate results of the time domain methods presented in section 2.2.

$$R^2 = \frac{\sum_{i=1}^{M}\sum_{i=1}^{N}\sum_{\tau=-P}^{Q} h_{ij}(\tau)\cdot\phi_{x_jy_i}(-\tau)}{\sum_{i=1}^{M} E[y_i(t)^2]} \quad (25)$$

References

Bendat JS, Piersol AG (1986) Random data: analysis and measurement procedures. Wiley, New York

Colgate JE, Hogan N (1988) Robust control of dynamically interacting systems. Int J Control 48:65–88

De Serres J, Milner TE (1991) Wrist muscle activation patterns and stiffness associated with stable and unstable mechanical loads. Exp Brain Res 86:451–458

Dolan JM, Friedman MB, Nagurka ML (1993) Dynamic and loaded impedance components in the maintenance of human arm posture. IEEE Trans Syst Man Cybern 23:698–709

Feldman AG (1966) Functional tuning of nervous system with control of movement or maintenance of a steady posture. III. Mechanographic analysis of the execution by man of the simplest motor tasks. Biofizika 11:667–675

Flash T (1987) The control of hand equilibrium trajectories in multi-joint arm movements. Biol Cybern 57:257–274

Flash T, Mussa-Ivaldi FA (1990) Human arm stiffness characteristics during the maintenance of posture. Exp Brain Res 82:315–326

Gomi H, Kawato M (1997) Human arm stiffness and equilibrium-point trajectory during multi-joint movement. Biol Cybern 76:163–171

Hogan N (1985) The mechanics of multi-joint posture and movement control. Biol Cybern 52:315–331

Hollerbach JM, Flash T (1982) Dynamic interactions between limb segments during planar arm movement. Biol Cybern 44:67–77

Hunter IW, Kearney RE (1982) Dynamics of human ankle stiffness: variation with mean ankle torque. J Biomech 15:747–752

Hunter IW, Kearney RE (1983) Two-sided linear filter identification. Med Biol Eng Comput 21:203–209

Kearney RE, Hunter IW (1982) Dynamics of human ankle stiffness: variation with displacement amplitude. J Biomech 15:753–756

Kearney RE, Hunter IW (1990) System identification of human joint dynamics. CRC Crit Rev Biomed Eng 18:55–87

Kearney RE, Stein RB (1997) Identification of intrinsic and reflex contributions to human ankle stiffness dynamics. IEEE Trans Biomed Eng 44:493–504

Kirsch RF, Kearney RE (1997) Identification of time-varying stiffness dynamics of the human ankle joint during an imposed movement. Exp Brain Res 114:71–85

Kirsch RF, Boskov D, Rymer WZ (1994) Muscle stiffness during transient and continuous movements of cat muscle: perturbation characteristics and physiological relevance. IEEE Trans Biomed Eng 41:758–770

Korenberg MJ (1988) Identifying nonlinear difference equation and functional expansion representations. Ann Biomed Eng 16:123–142

MacNeil JB, Kearney RE, Hunter IW (1992) Identification of time-varying biological systems from ensemble data. IEEE Trans Biomed Eng 39:1213–1225

Marmarelis PZ, Marmarelis VZ (1978) Analysis of physiological systems. Plenum Press, New York

Marple SL (1981) Efficient least squares FIR system identification. IEEE Trans Acoustics: Speech Signal Proc 29:71–85

McIntyre J, Mussa-Ivaldi FA, Bizzi E (1996) The control of stable arm postures in the multi-joint arm. Exp Brain Res 110:62–73

Morasso P (1981) Spatial control of arm movements. Exp Brain Res 42:223–227

Mussa-Ivaldi FA, Hogan N, Bizzi E (1985) Neural, mechanical, and geometric factors subserving arm posture in humans. J Neurosci 5:2732–2743

Perreault EJ, Acosta AM, Kirsch RF, Crago PE (1997) Using estimates of dynamic endpoint stiffness to quantify the effects of triceps functional neuromuscular stimulation. International Functional Electrical Stimulation Society Conference, Vancouver

Rack PMH, Westbury DR (1974) The short range stiffness of active mammalian muscle and its effect on mechanical properties. J Physiol 240:331–350

Shadmehr R, Mussa-Ivaldi FA, Bizzi E (1993) Postural force fields of the human arm and their role in generating multijoint movements. J Neurosci 13:45–62

Soechting JF, Lacquaniti F (1981) Invariant characteristics of a pointing movement in man. J Neurosci 1:710–720

Tsuji T, Morasso PG, Goto K, Ito K (1995) Hand impedance characteristics during maintained posture. Biol Cybern 72:475–485

Welch PD (1967) The use of fast fourier transform for the estimation of power spectra: a method based on time averaging over short, modified periodograms. IEEE Trans Audio Electroacoustics 15:70–73

Westwick DT, Kearney RE (1997) Identification of physiological systems: a robust method for non-parametric impulse response estimation. Med Biol Eng Comp 35:83–90c